Geophysical Research Letters

RESEARCH LETTER
10.1029/2025GL117900

Calving as a Source of Acute and Persistent Kinetic Energy to Enhance Submarine Melting of Tidewater Glaciers

M. F. Shaya[1], J. D. Nash[2], E. C. Pettit[2], J. M. Amundson[3], R. H. Jackson[4], D. A. Sutherland[5], and D. Winters[6]

[1]Department of Earth and Space Sciences, University of Washington, Seattle, WA, USA, [2]College of Earth, Ocean, and Atmospheric Sciences, Oregon State University, Corvallis, OR, USA, [3]Department of Natural Sciences, University of Alaska Southeast, Juneau, AK, USA, [4]Department of Earth and Climate Sciences, Tufts University, Medford, MA, USA, [5]Department of Earth Sciences, University of Oregon, Eugene, OR, USA, [6]Department of Electrical and Computer Engineering, Portland State University, Portland, OR, USA

Key Points:

- Buoyant potential energy from a submarine calving event energizes near-terminus currents (~ 15%), turbulence (~75%), and waves (<5%)
- Fluid entrainment during iceberg rise is an important control on the partitioning of energy into the fjord
- Enhanced near-terminus water speeds increase melt rates by a factor of 5 during the event and a factor of 1.7 for 5 hr after

Supporting Information:

Supporting Information may be found in the online version of this article.

Correspondence to:

M. F. Shaya,
mshaya@uw.edu

Citation:

Shaya, M. F., Nash, J. D., Pettit, E. C., Amundson, J. M., Jackson, R. H., Sutherland, D. A., & Winters, D. (2025). Calving as a source of acute and persistent kinetic energy to enhance submarine melting of tidewater glaciers. *Geophysical Research Letters*, *52*, e2025GL117900. https://doi.org/10.1029/2025GL117900

Received 5 JUL 2025
Accepted 9 SEP 2025

Abstract Calving icebergs at tidewater glaciers release large amounts of potential energy. This energy—in principle—could be a source for submarine melting, which scales with near-terminus water temperature and velocity. Because near-terminus currents are challenging to observe or predict, submarine melt remains a key uncertainty in projecting tidewater glacier retreat and sea level rise. Here, we study one submarine calving event at Xeitl Sít' (LeConte Glacier), Alaska, to explore the effect of calving on ice melt, using a suite of autonomously deployed instruments beneath, around, and downstream of the calving iceberg. Our measurements captured flows exceeding 5 m/s and demonstrate how potential energy converts to kinetic energy (E_K). While most energy decays quickly (through turbulence, mixing, and radiated waves), near-terminus E_K remains elevated, nearly doubling predicted melt rates for hours after the event. Calving-induced currents could thus be an important overlooked energy source for submarine melt and glacier retreat.

Plain Language Summary For glaciers that terminate in fjords, the melting of ice in the ocean water can lead to glacier retreat and sea level rise. The rate of melting depends on water currents and turbulence, which transport heat and salt from the ocean to the ice. Large chunks of ice detaching from the glacier, called iceberg calving, are a source of energy that can affect water circulation. In this study, we present new observations of changes to fjord circulation after a large iceberg calved from the submerged part of Xeitl Sít (LeConte Glacier), Alaska. Instruments deployed close to the glacier terminus by remotely operated boats measured the water currents beneath and around the calving iceberg. As the buoyant iceberg moved from the bottom of the fjord to the surface, it released enough energy to bring water in a standard backyard swimming pool to a boil. This energy flowed into surface waves, slower-moving and larger amplitude internal waves, mixing of the water column, as well as faster and more strongly varying water velocities. The water currents remained faster for hours after calving, implying that melt rates also intensified during this time. These results suggest that calving may be an important contributor to melting.

1. Introduction

Mass loss from glaciers and ice sheets is a leading cause of current (Zemp et al., 2025) and projected sea level rise (Marzeion et al., 2020; Rounce et al., 2023). Significant uncertainty for these projections stems from gaps in understanding of ice-ocean interactions (Edwards et al., 2021). A better understanding of frontal ablation processes (calving, submarine melting, and feedbacks between the two) is critical for improving projections of glacier change and resulting sea level rise (Huss & Hock, 2015; Malles et al., 2023). Studies have investigated how melt influences calving (e.g., Alley et al., 2023), however the potential for calving to influence fjord dynamics that may feed back to melting has only recently been recognized (e.g., Gräff et al., 2025; Meredith et al., 2022).

Calving occurs when new or preexisting fractures propagate through the ice due to gravitational stresses (undercut ice), buoyant stresses (overcut ice), shearing, or longitudinal tension (Alley et al., 2023). Iceberg calving and capsize are known to be significant sources of energy in tidewater glacier fjords (Amundson et al., 2008; Burton et al., 2012; Lüthi & Vieli, 2016; MacAyeal et al., 2011), although the transfer of energy between iceberg and fjord depends on the calving process. For example, serac failure, or the collapse of columns of ice above the waterline (Bézu & Bartholomaus, 2024), leads to waves, big splashes and projectile ice flying 100s of meters

downstream, but perhaps little effect on submarine conditions. This contrasts with full-thickness buoyant calving (James et al., 2014) and buoyant ice-foot calving (Benn & Åström, 2018; Benn et al., 2007). Also termed submarine calving, this last calving style occurs when a protruding ice foot (Abib et al., 2023) snaps off and rises to the surface under the force of buoyancy (Hunter & Powell, 1998). Submarine calving has a unique potential to directly affect the waters deep in the fjord because the icebergs typically detach near the bed (indicated by the presence of basal ice, O'Neel et al., 2003; Hubbard et al., 2009).

In energetic fjords, submarine melting of tidewater glaciers is controlled by the temperature and velocity of the boundary layer adjacent to the submerged ice, which set transfer rates of heat and salt at the glacier-ocean interface (McPhee et al., 1987). Although temperature is relatively easy to observe, near-terminus velocities are challenging to measure. While it is accepted that currents near the terminus can be appreciable (e.g., Cowton et al., 2015; Jackson et al., 2020; Kienholz et al., 2019), they are often believed to be energized primarily by subglacial discharge plumes (Slater et al., 2018), locally-energized internal waves (Cusack et al., 2023; Gräff et al., 2025), and melt-driven circulation (Zhao et al., 2022).

Here, we argue that (a) submarine calving is an important source of energy in tidewater glacier fjords and (b) a significant fraction of this energy is available to energize near-terminus currents and enhance melt. We present a unique set of observations at Xeitl Sít' (LeConte Glacier, Alaska) that capture a submarine calving event from below. We quantify the energy transferred from a buoyant iceberg to the fjord and show that the energy primarily flows to elevated current speeds and turbulent mixing and dissipation. While much of the energy decays over a few minutes, we observe a persistent (>5 hr) increase to the kinetic energy of near-terminus waters, which has implications for submarine melting.

2. Observations of a Single Calving Event at Xeitl Sít' Glacier

At ∼16:35 UTC on 6 September 2018, a submarine calving event occurred at Xeitl Sít'. The event was captured by time-lapse photography from a vantage point above the glacier (30-s intervals, see Amundson et al., 2020; Kienholz et al., 2019), along with 300 kHz acoustic Doppler current profilers (ADCPs) and conductivity temperature depth (CTD) sensors on three moorings (Figure 1). Moorings M-South and M-North were deployed ∼100 m from the glacier terminus by remotely-operated kayaks (Nash et al., 2017; Cusack et al., 2023) with upward-looking ADCPs recording velocity profiles in 4-m bins every 2–3 s. The 4-beam RDI Workhorse on M-South was 14 m above the bottom and almost directly beneath the calving event; the 5-beam RDI Sentinel-V on M-North was 55 m above the bottom and 170 m north of the main event. M-Distant was a traditional oceanographic mooring (two 4-beam ADCPs at mid-depth, distributed CTD and temperature sensors) deployed ∼400 m from the terminus on a 170 m deep morainal bank (see Eidam et al., 2020, for the fjord bathymetry).

The first sign of calving occurred at 16:35:03, when pressure recorded at M-North (Figures 2d and 2e) dropped (the ocean-surface lowered). At 16:35:14, the M-South ADCP pitched up (Figure S1 in Supporting Information S1). Over the next minute, the ADCP recorded highly-variable pitch and roll and along-beam velocities in excess of 3 m/s in all 4 beams (Figure S2 in Supporting Information S1). The ADCP also dropped in depth from 146 to 153 m and remained ∼8 m deeper even after calving subsided; we hypothesize the iceberg hit the mooring and moved it into deeper water.

From 16:35:30 to 16:35:45, the ADCP pitch and roll stabilized, and beams 2 and 4 (which were less affected by acoustic artifacts) recorded average along-beam velocities of 2–3 m/s (Figure 2c, blue dots). It was not until 16:35:55 that time-lapse cameras imaged the iceberg at the surface. By the next image frame (30-s later), the iceberg had broken into two large pieces (and many smaller fragments) and rolled. The iceberg then moved southwest at 1 m/s until it grounded on the south shore at 16:40, 5 min after calving.

Before calving, flow at all moorings was weakly toward the glacier (east) at depths >30 m and away from the glacier (west) at the surface (Figures 1f and 1h), consistent with expected subglacial plume-driven dynamics. The rising iceberg energized the entire water column, producing >2 m/s velocities at M-South and M-North in the 2 min following the start of calving. The strongest velocities were short lived: by 16:38 (3 min after calving), they relaxed to less than 1 m/s.

All three moorings recorded strong undulating velocities after calving (Figures 1f–1j). At M-North, for example, the upper half of the water column moved away from the calving site at more than 1.5 m/s in a pulse that lasted over 30 s. Velocities reversed 1 min later, moving south and up toward the void left by the outbound iceberg.

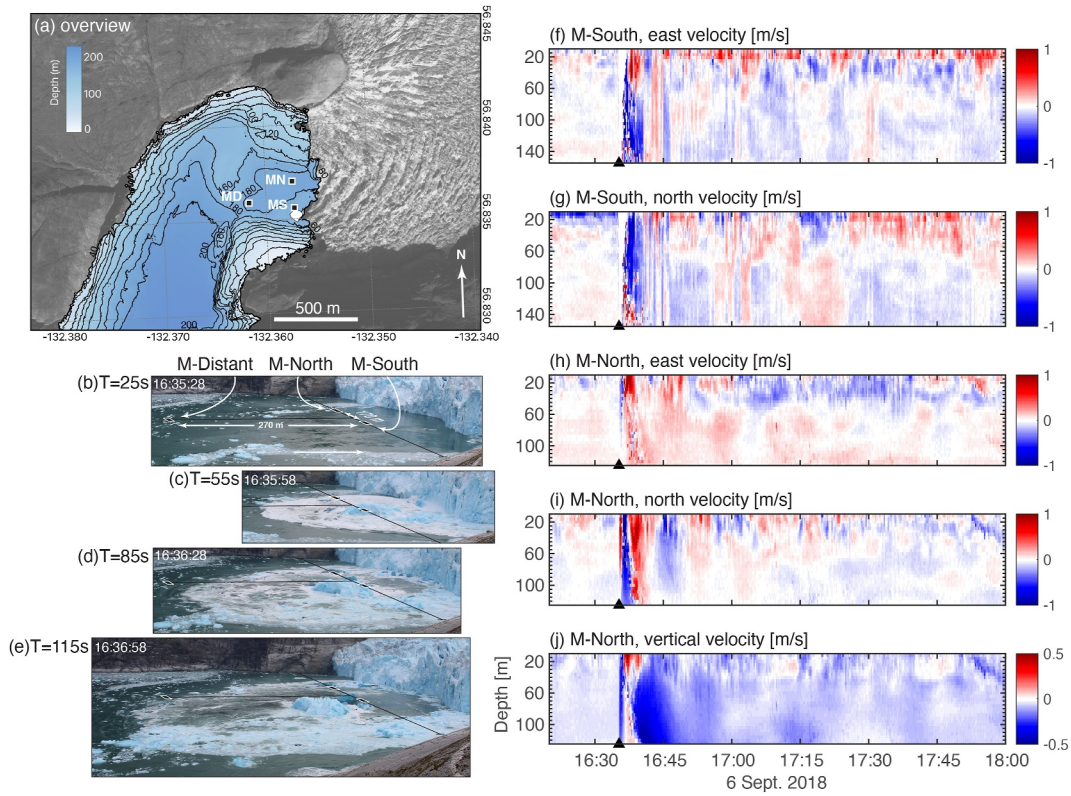

Figure 1. Overview of the calving event. (a) A map of moorings M-Distant (MD), M-North (MN), and M-South (MS) relative to the glacier terminus. The white patch near M-South represents the iceberg outline after its initial rise, as digitized from time-lapse imagery. The background image is a Worldview 13 September 2018 UTM projection with latitude and longitude indicated. (b–e) Photographs spanning the first 2 min of the calving event. (f–j) ADCP-derived velocities from M-South and M-North. Note the oscillating velocities after calving. The strong downward velocities at M-North (j) likely represent a combination of resettling of entrained waters and raining down of sediment lifted by the iceberg.

These lasted until ~16:37:30, at which point the flow reversed again, reaching sustained speeds of 0.85 m/s for several minutes. These reversals appear to be the beginning of oscillations (Section 3.5) that persisted over the next several hours, visible both in surface displacements (Figure 2d) and currents (Figures 1f–1j).

3. Partitioning of the Energy Budget

In the following sections, we analyze the energy transfer pathways during the submarine calving event, which are summarized graphically in Figure 3f. These calculations paint a broadly consistent picture of energy flow from the iceberg to the ocean and provide a framework for analyzing the impacts of calving on fjord processes.

3.1. Submarine Calving Releases Buoyant Potential Energy

The potential energy (E_P) released by submarine calving is the work done by buoyant and gravitational forces as the center of mass of an iceberg moves from initial depth z_i (here 145 m, based on an iceberg height of 50 m and fjord depth of 170 m) to a final elevation z_f (here 25 m). Thus,

$$E_P = g\int_{z_i}^{z_f} \left(\rho_w V_i'(z) - \rho_i V_i\right) dz, \tag{1}$$

where V_i is the total volume of the iceberg and $V_i'(z)$ is the submerged volume of ice. We use an ice density of $\rho_i = 917$ kg/m^3. Due to the large density difference between ice and water, we neglect fjord stratification and assume a uniform water density $\rho_w = 1022$ kg/m^3.

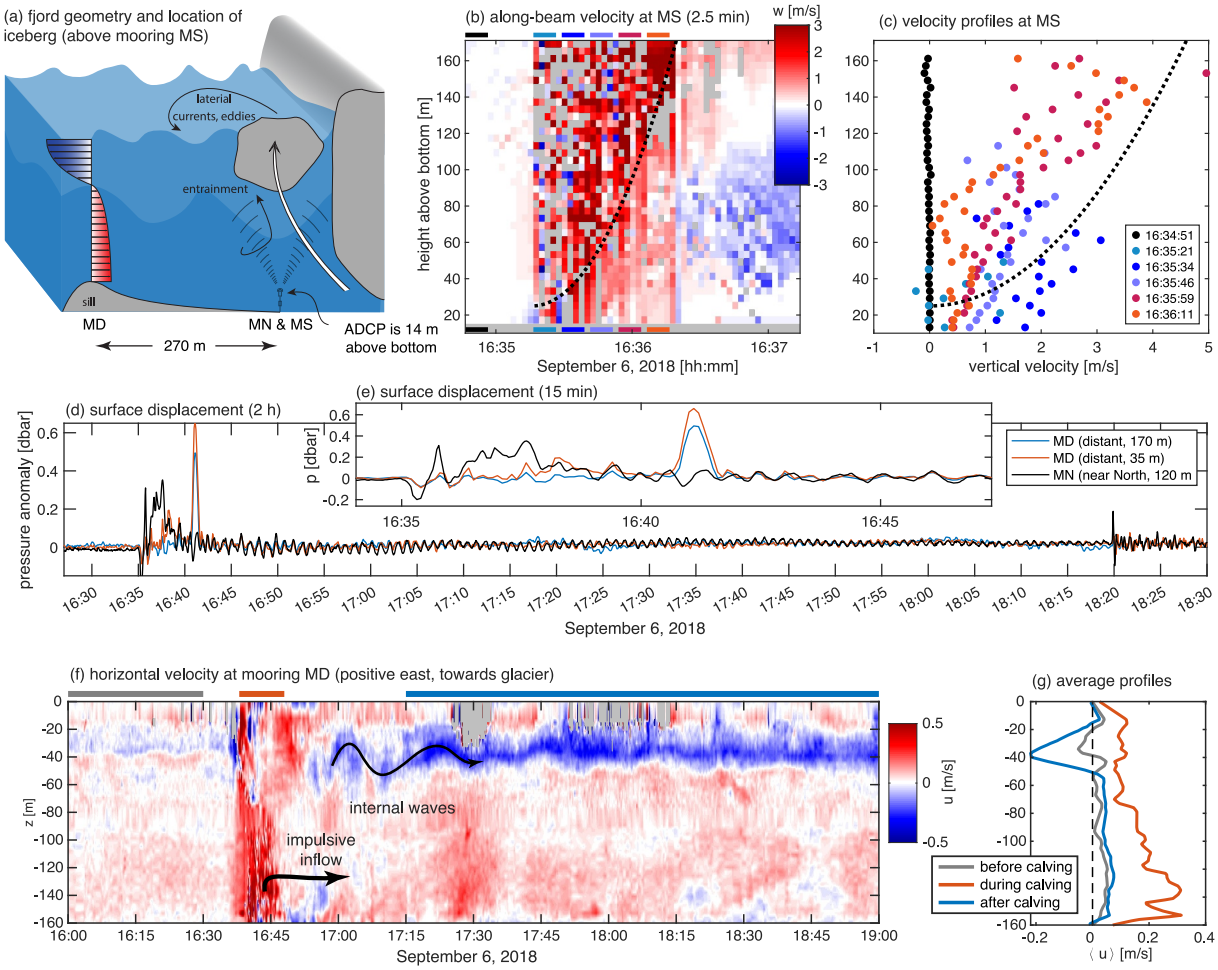

Figure 2. Energy transfer between the rising iceberg and the fjord. (a) Fjord geometry, iceberg and mooring locations. (b) Upward velocity timeseries at M-South in the 2 min following calving. Plotted is the along-beam velocity averaged over the two beams directed toward the rising iceberg (red upward). The black dotted line shows a theoretical rise curve assuming 13× entrainment of water. (c) Profiles of the same data as in panel (b), with along-beam velocities averaged over 12.5 s blocks (black dots are before calving, colored dots are after). The black dotted line is the theoretical rise rate. Over the expected ∼1 min iceberg rise duration, the peak velocities move from the lower half of the water column (blue dots, ≲35 s post-calving) to the top half (red dots, 35.7–60 s post-calving). (d) Pressure anomaly time-series at M-North and M-Distant showing the initial pressure impulse and the persistent seiche wave. (e) Zoom-in on the first 15 min of the pressure anomaly. (f) Eastward component of velocity at M-Distant. (g) Velocities averaged over the colored time bars in (f), showing a deep impulse toward the glacier during calving and an enhanced near-surface outflow after.

We use time-lapse imagery to estimate the iceberg dimensions as $V_i \approx 100 \times 100 \times 50\ \mathrm{m}^3$, and recognize this is subject to significant error due to lack of observations below the waterline. We estimate ±50% as a reasonable volume uncertainty. We neglect uncertainty in the distance traveled by the iceberg $(z_f - z_i)$ because it acts oppositely to changes in V_i: a smaller iceberg (with lower E_P) must travel a greater distance from the fjord bottom (acting to increase E_P).

Based on these numbers, we estimate the iceberg released $(6 \pm 3) \times 10^{10}$ J of potential energy, where our uncertainty stems entirely from the iceberg volume. For context, the buoyant energy flux for 350 $\mathrm{m}^3\ \mathrm{s}^{-1}$ of subglacial discharge (Sutherland et al., 2019, late-summer high estimate) is 4.6 $\times\ 10^{10}$ J/hr. In under a minute, the calving event releases the same order of magnitude of energy as does an hour of strong subglacial discharge forcing (see Section S3.1 in Supporting Information S1).

3.2. Fluid Entrainment as a Primary Mechanism for Energy Transfer

In the absence of water entrainment during the iceberg rise, all E_P would convert to iceberg kinetic energy, which implies a 17 s duration rise and 15 m/s terminal velocity. Instead, the M-South ADCP, which was located beneath

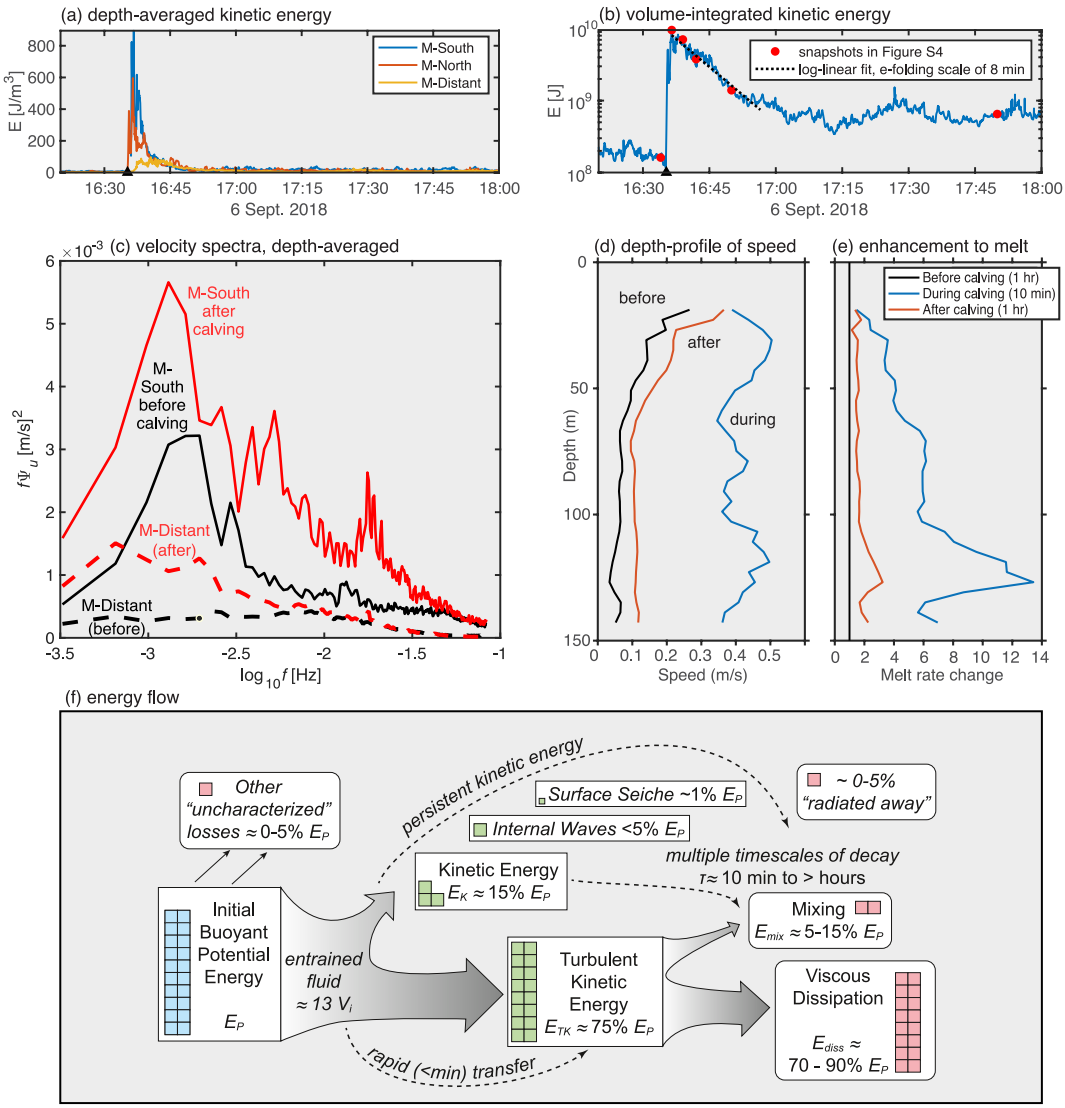

Figure 3. Elevated kinetic energy levels in the fjord following calving drive melting. (a) Depth-averaged kinetic energy density calculated from the observed current speeds at each mooring. (b) The volume-integrated kinetic energy, as explained in Section S3.2 in Supporting Information S1. (c) Variance-preserving spectra before and after calving at M-Distant and M-South. (d) Depth-averaged speed at M-South before, during, and after calving. (e) Factor enhancement to the melt rate calculated from the relative change in speed during and after calving. (f) Schematic of energy transfer during the submarine calving event, with colored boxes indicating quantity of each source (blue), transient/flow (green), and loss terms (red).

the iceberg and likely captured a combination of the rising iceberg and water entrained in its wake, recorded near-surface velocities of 3–5 m/s after calving (Figures 2b and 2c). Assuming a peak iceberg velocity of 5 m/s, the iceberg kinetic energy was at most 10% of E_P, implying that 90% of the energy flows to the water before the iceberg reaches the surface. This result aligns with the laboratory experiments of Burton et al. (2012), who observe an immediate transfer of most (85%) of the energy from the iceberg to the surrounding fluid.

The initial energy transfer occurs through entrainment of water during the iceberg rise. We compute an idealized iceberg trajectory from the force balance ($F = ma$) of the rising iceberg using the concept of "added mass" (e.g., Tsai et al., 2008) to set $m = V_i\rho_i + V_w\rho_w$ for an entrained volume of water V_w. The iceberg velocity is the integrated acceleration:

$$v_{\text{berg}}(t) = \frac{1}{\rho_i + f_e\rho_w}(\rho_w - \rho_i)\, gt, \tag{2}$$

where $f_e = V_w/V_i$ is the entrainment fraction. Using $f_e = 13$ (see below), yields a rise time of ~60 s and a maximum speed of 4.8 m/s at the surface (Figures 2b and 2c), consistent with the time it took for the iceberg to reach the surface and the ADCP-observed velocities.

The rising iceberg and entrained fluid moved deep waters to the surface, drawing new water over the sill. Our observations capture this replenishment, both as deep southward flow at M-North (170 m to the North), and also as inflow at M-Distant (270 m to the West). At M-Distant, strong toward-glacier flows (red) are observed in the bottom 120 m (Figure 2f), delayed only by the time for barotropic wave propagation ($\ell/\sqrt{gH} \sim 10$ s for distance $\ell = 400$ m and mean depth $H = 180$ m). For the first 5 minutes (until 16:40), this inflow increased smoothly (to about 0.3 m/s), then abruptly broke into a stronger and highly turbulent flow (from 16:40 to 16:47) with mean toward-terminus velocities and fluctuations exceeding 0.5 m/s. Integrating the excess inflow in time (between 16:34 and 16:48), below 40 m depth, and assuming the mooring is representative of a 500 m wide swath (the fjord is 1,000 m wide at the surface), we estimate that the calving event drew $V_w = 6.7 \times 10^6$ m^3 (or roughly 13× the volume of the iceberg) of deep water over the sill and toward the terminus. All of these "induced flows" have kinetic energy and are sinks for the iceberg's initial E_P.

3.3. Kinetic Energy Distribution and Evolution

As a crude estimate of the total kinetic energy, E_K, imparted to fjord currents, we spatially interpolate the depth-integrated kinetic energy measured at the three moored ADCPs, assuming radial symmetry in the half plane down-fjord of the terminus (see Section S3.2 in Supporting Information S1). Figure S4 in Supporting Information S1 shows snapshots of the extrapolated energy field at the times corresponding to the red dots in Figure 3b. The spatial integral of this extrapolated energy field provides a total estimated E_K as a function of time (Figure 3b and Figure S5 in Supporting Information S1).

While this back of the envelope extrapolation glosses over many details, it captures several salient aspects of the energy budget, namely:

- The observed peak E_K occurred 1 min after calving and was 9×10^9 J, which is only about 15% (10%–30% given uncertainties in V_i) of the total estimated E_P.
- The peak E_K represents an over 50-fold increase in energy relative to the hour before calving.
- Over the first 20 min, the energy decayed with a $\tau_e = 8$-minute e-folding timescale: $E_K(t) = E_0 \exp(-(t - t_0)/\tau_e)$ (dotted black line in Figure 3b).
- After the initial decay, E_K remained elevated by a factor of 3 for 5 hours.

The lasting increase to kinetic energy suggests that calving can induce a persistent circulation in addition to enhanced current variability (Figures 3c and 3d). An alternative explanation is that the higher velocities result from changes to the subglacial discharge forcing, whether through increased afternoon discharge flux or through a calving-related change to the outlet location. However, the E_K from 17:00 to 21:00 directly after the calving event is 2.7× greater than on the following day, suggesting that subglacial discharge effects are at most a small contributor to the elevated speeds.

3.4. Energy Flow to Turbulent Mixing and Dissipation

Based on the observed rise velocity (Figures 2b and 2c), only 10% of E_P was transferred to the iceberg itself; 90% went elsewhere. Given that our extrapolated E_K accounts for only ~15% of the total energy, where did the remainder of the energy go? While some energy radiates in surface and internal waves (Section 3.5), we argue that ~75% of E_P drives irreversible mixing and viscous dissipation—two distinct sinks for the turbulent kinetic energy (E_{TK}) contained in eddies, trapped waves (e.g., MacAyeal et al., 2012), and other chaotic motions energized by the calving event.

Mixing: Turbulent mixing acts as a sink of E_{TK} by irreversibly raising the gravitational potential energy of a closed system. Previous estimates vary for the fraction of calving-related energy that contributes to mixing. Burton et al. (2012) calculate that only 5% of the energy of a typical calving event at Sermeq Kujalleq (Jakobshavn Isbræ) could completely mix the innermost 1000×5000 m^2 of the proglacial fjord. Meredith et al. (2022) estimate that 9%–35% of the potential energy released in a large calving event flowed to mixing in Börgen Bay, Antarctica.

Following Burton et al. (2012), we calculate the energy required to completely mix the near-terminus water, E_{mix}, as the difference in potential energy between the initial (stratified) and homogenized (fully mixed) water column. Assuming a uniform fjord depth of 180 m, we use CTD casts collected near M-South (Jackson et al., 2020) to estimate the energy needed for mixing (per unit area) as $E_{\mathrm{mix}}/A = 5.3 \times 10^4$ J/m^2 (see Section S3.3 in Supporting Information S1).

We expect mixed water to spread out and flow down-fjord at its depth of neutral buoyancy (expected to be ~60 m, Figure S6 in Supporting Information S1), which is observed as a substantial increase in outflow after calving (westward flow at ~40 m depth at M-Distant, Figure 2f). The increase in exported fluid (integrated over the outflow depth) is 3 m^2/s (Figure 2g); when integrated over a 500 m wide sill and over 3 hr, this yields 1.6×10^7 m^3 of excess fluid exported, equivalent to a 30 m thick layer spanning the entire 500 m × 1,000 m "near-terminus" region (and about double the 7×10^6 m^3 of fluid entrained during calving/iceberg rise). Assuming mixing occurs across the entire water column, fully mixing this volume would require $E_{\mathrm{mix}} = 4.8 \times 10^9$ J of energy—about 11% of the available E_{TK} and ~8% (5–15% with uncertainty bounds of V_i) of E_P, and not inconsistent with stratified shear-flow mixing efficiencies for which 20% is a typical upper bound (Gregg et al., 2018).

Dissipation: A substantial fraction of E_{TK} cascades toward viscous scales in one eddy-turnover time $\sim \ell/U$, where ℓ and U are the length and velocity scales characteristic of the turbulent eddy. This yields a turbulent dissipation rate $\epsilon \sim U^3/\ell$ (Tennekes & Lumley, 1972). In our case, the initial calving creates an upward-rising turbulent flow in which its ~4 m/s characteristic velocity and 180 m eddy size (set by the rise distance and water depth) determine an initial turbulent dissipation rate of $\epsilon \sim U^3/\ell = 0.35$ W/kg. If all the water entrained by the rising iceberg, roughly $V_w = 6.7 \times 10^6$ m^3 (Section 3.2), were associated with this idealized eddy, the volume-integrated dissipation rate is 2.4×10^9 W. In other words, turbulence dissipates energy at an initial $1/e$ timescale of just 25 s. A toy model (Figure S8 in Supporting Information S1) suggests that turbulent decay could reduce the turbulent velocities to 1 m/s in approximately 2.5 min. Thus, turbulence is a first-order sink in the energy budget in the initial moments after calving, with the energy ultimately flowing to heat via viscosity. Note that dissipative heating is inconsequential to melt, as the associated temperature rise is negligible (~0.002 K if distributed evenly within V_w).

3.5. Radiated Waves

Surface gravity waves are a ubiquitous and often dramatic remotely-sensed sign of sub-aerial calving (Amundson et al., 2008, 2010; Lüthi & Vieli, 2016; Wagner et al., 2019). This particular submarine calving event generated both surface and internal waves, however waves represent only a small fraction of E_P.

Surface Waves: The first sign of calving was a lowering of the sea-surface (20 cm at M-North and 8 cm at M-Distant 5 s later; Figure 2e), likely in response to the raised sea surface above the rising iceberg near M-South (Figure 1b). About 30 s later, the sea surface rebounded and was elevated by 31 and 4 cm at M-North and M-Distant, respectively. Several minutes of confused seas ensued, along with a solitary peak in the pressure at M-Distant at 16:40:30.

For the following 90 min, sea-surface oscillations persisted with a 56 s period and similar phase at all moorings (Figure 2d). Post-calving velocity spectra (Figure 3c) also show elevated variance at 1-min periods ($f = 10^{-1.8}$ Hz). We interpret these surface waves as a cross-fjord seiche, similar to those observed by Amundson, Clinton, et al. (2012) and Walter et al. (2013) and with a theoretical resonance period $\tau = 2L/\sqrt{gH}$ for fjord width L and depth H (Rabinovich, 2009). While irregular geometry and ice melange can affect τ (MacAyeal et al., 2012), the observed seiche period of $\tau = 56$ s is consistent with Xeitl Sít' fjord geometry, taking $L = 1,070$ m and $H = 150$ m. The initial M-North pressure disturbance has a period of ~1 min (30 s interval from trough to peak), meaning that the impulse from calving can directly energize the seiche frequency band.

Total seiche energy depends on amplitude and along-fjord extent, both of which are poorly constrained by our data. Assuming an amplitude of 10 cm and a 1,000 m down-fjord extent (see Section S3.5 in Supporting Information S1), we estimate a seiche energy of 0.2% of E_P.

Internal Waves: For the next 1–2 hr, a series of decaying oscillations with 10–15 min period were evident in the velocity (Figure 2) and their spectra (peak near $f = 10^{-2.8}$ Hz; Figure 3c). The upper and lower parts of the water

column were often out-of-phase, characteristic of low-mode internal waves, also observed by Cusack et al. (2023). Enhanced motion with longer-periods (~15 min and greater) also emerges after calving in all mooring records, likely representing a superposition of internal waves, eddies, and small gyres not present before calving. To estimate the energy associated with the ~10 m amplitude internal waves observed at M-Distant (Figure 2), we solve the Taylor Goldstein equation (Drazin & Reid, 2004) to compute the first-mode group speed ($c_g = 0.47$ m/s). Generously assuming that waves propagate for 2000 s across a 1,000 m wide fjord, the total energy transported down-fjord by internal waves is 1×10^9 J, a small fraction of the total energy released (see Section S3.6 in Supporting Information S1).

4. Implications

Moored observations from beneath and around a submarine calving event have provided a unique opportunity to quantify how energy flows from a buoyantly rising iceberg into fjord waters. We summarize the flow of energy in Figure 3f. We estimate that only 10% of the available buoyant energy (E_P; blue boxes) is imparted to the rising ice; this energy is quickly lost to waves and turbulence when the iceberg comes to "rest" at the ocean surface. The other 90% of E_P is imparted into fluid entrained around the rising iceberg; because deep fjord waters are nutrient rich (Williams et al., 2021), this calving-driven upwelling may affect nutrient availability and primary production. To replenish the rising waters, a similar amount of water is drawn over the sill at depth, energizing fluid velocities across the near-terminus basin (green boxes). Most of this energy dissipates in seconds to minutes through turbulent processes; however, ~15% of E_P flows to long-lasting currents (gyres, eddies, and internal waves) which dissipate on timescales ranging from $\tau_e = 8$ min (observed e-folding scale for E_K over the first 20 min) to hours (based on the persistence of E_K for the 5 hr after calving).

Through this amplified fjord circulation, iceberg calving enhances submarine melting. Taking melt rate to be proportional to the near-terminus water speed (McPhee et al., 1987) and assuming velocities measured ~100 m from the terminus are representative of the boundary-layer flows, Figures 3d and 3e show both the acute (10 min) and persistent (1 hr) enhancement to current speeds and predicted melt rates at M-South compared to the one hour period before calving. Mean water speeds at all three moorings increased 1.7-fold (corresponding to a 3-fold increase in the "volume-integrated" E_K) in the 5 hr after calving, resulting in a near-doubling of predicted submarine melt rates that likely extends across much of the terminus face.

If all available E_P from the submarine calving event were converted directly (and only) to thermal energy, it could melt 200 ± 100 m^3 of ice—less than 2 mm of melt across the submerged terminus. But by enhancing near-terminus velocities, which drive heat and salt fluxes across the ice-ocean interface, the calving event has a ~50× greater effect on melt. We estimate this melt contribution by assuming a spatially uniform pre-calving velocity of 0.07 m/s (based on average mooring speeds before the event) and post-calving velocity of 0.12 m/s. Taking a constant fjord temperature of 7°C and salinity of 28, the 3-equation melt parameterization with standard coefficients (Holland & Jenkins, 1999) predicts melt rates to increase from 0.6 to 1.0 m/day. Over 5 hr, this change amounts to an extra 9 cm of predicted melt due to calving, which we consider a lower bound (Weiss et al., 2025, find melt at Xeitl Sít' to be on average 2× larger than predicted by standard coefficients). Energy flow to fjord currents is thus an efficient way to enhance melt, although the strength of this amplification will scale with fjord temperatures.

The particular calving event studied here is large, but not exceptional for Xeitl Sít', suggesting that calving-induced melting could represent an appreciable fraction of total melt rates (found to be 6 m/day in summer by Sutherland et al., 2019). Taking a mean calving flux at Xeitl Sít' of ~30 m^3/s water equivalent (Jackson et al., 2022), we estimate that the ice discharged in the event represents <20% of the daily calving flux. O'Neel et al. (2003) visually monitored daytime calving at Xeitl Sít' in May 1999; they observed 14 massive calving events, with a typical sequence involving sub-aerial calving, followed by submarine calving in the middle portion of the terminus, then submarine calving of deep basal ice. Their results suggest that large submarine calving events of the type studied here could occur every ~2–3 days, although this frequency may be highest in spring when the terminus undergoes seasonal retreat (e.g., Eidam et al., 2020; Figure 3) while submarine melt rates remain lower (e.g., Sutherland et al., 2019; Figure 3).

In general, the energy transfer pathways for calving events likely depend on the calving style (submarine, sub-aerial, full-thickness, etc.), the iceberg size, shape, and other interactions with existing motions in the fjord. We expect the greatest melt enhancement when a calving event can persistently amplify currents. For the

submarine calving event studied here, we identify fluid entrainment during iceberg rise as a key process that imparts momentum to the fjord and sets eddies in motion. Experiments and models of iceberg capsize (Amundson, Burton, & Correa-Legisos, 2012; Bonnet et al., 2020) similarly emphasize hydrodynamic effects, which rapidly impart energy to the water and can generate high-velocity turbulent flow (De Pinho Dias et al., 2025). In contrast, sub-aerial events can input more energy for the same volume of ice and distance traveled (because of the greater density difference between ice and air), but we speculate that their impact to circulation—and hence submarine melting—will be less. And while large submarine events can energize long-lasting currents, concurrent small calving events may destructively interfere in the fjord, generating turbulence but not persistent motions.

Our findings—that a submarine calving event at Xeitl Sít' energizes near-terminus currents and significantly enhances melting—show that the feedbacks between calving and submarine melting may be more complicated than previously understood. Localized submarine melting of glacier termini has been found to undercut portions of the terminus and trigger calving (Benn et al., 2023; Goliber & Catania, 2024; Slater et al., 2018). If submarine calving amplifies submarine melt, and submarine melt can amplify sub-aerial calving, linking parameterizations for calving and submarine melt in models may be necessary.

Conflict of Interest

The authors declare no conflicts of interest relevant to this study.

Data Availability Statement

The time-lapse imagery of the fjord is archived at the Arctic Data Center (Amundson, 2019, https://doi.org/10.18739/A27W6754N) as are the Robotic Oceanographic Surface Sampler conductivity temperature depth profiles (Sutherland et al., 2020, https://doi.org/10.18739/A2WW77125). Mooring data are archived on Zenodo (Nash et al., 2025, https://doi.org/10.5281/zenodo.16923006).

Acknowledgments

We thank the participants of the 2018 LeConte Glacier field efforts, including the crew of the M/V Amber Anne and the engineers—Jasmine Nahorniak, June Marion, Nick McComb, Anthony Grana, and Corwin Perren—who developed the remotely operated mooring deployment system. We especially thank Petersburg residents Scott and Julie Hursey for recovering instruments from M-South, which failed to release on command (due to noisy fjord conditions) by the time our cruise ended, but did release during a calving event on September 18, sent a satellite signal, and drifted down fjord. We also thank two anonymous reviewers, T.J. Fudge, and Dominik Gräff for their helpful comments on the manuscript. The risky deployment of moorings at the terminus was funded through a grant by the National Geographic Society (CP4-171R-17). We especially thank Paul Devine and Teledyne RD Instruments for their loan of a Sentinel V ADCP, knowing the deployment was risky and loss was possible. The ship time and all associated equipment, development, and analysis was funded by the U.S. National Science Foundation Office of Polar Programs (Grants 1503910, 1504191, 1504288, 1504521), and the Office of Naval Research (Grants N00014-14-1-0490 and N0001417-1-2864). M. Shaya was initially supported through the Oregon State University College of Earth Ocean and Atmospheric Sciences NSF-funded Research Experience for Undergraduates in 2019 (OCE-1758000). This work was also partially supported by the U.S. National Science Foundation Center for Oldest Ice Exploration (NSF COLDEX), an NSF Science and Technology Center (NSF 2019719).

References

Abib, N., Sutherland, D. A., Amundson, J. M., Duncan, D., Eidam, E. F., Jackson, R. H., et al. (2023). Persistent overcut regions dominate the terminus morphology of a rapidly melting tidewater glacier. *Annals of Glaciology*, *64*(90), 1–12. https://doi.org/10.1017/aog.2023.38

Alley, R., Cuffey, K., Bassis, J., Alley, K., Wang, S., Parizek, B., et al. (2023). Iceberg calving: Regimes and transitions. *Annual Review of Earth and Planetary Sciences*, *51*(1), 189–215. https://doi.org/10.1146/annurev-earth-032320-110916

Amundson, J. M. (2019). LeConte Glacier time-lapse photos, LeConte Glacier, Alaska, 2018 [Dataset]. *Arctic Data Center*. https://doi.org/10.18739/A27W6754N

Amundson, J. M., Burton, J. C., & Correa-Legisos, S. (2012). Impact of hydrodynamics on seismic signals generated by iceberg collisions. *Annals of Glaciology*, *53*(60), 106–112. https://doi.org/10.3189/2012/AoG60A012

Amundson, J. M., Clinton, J. F., Fahnestock, M., Truffer, M., Lüthi, M. P., & Motyka, R. J. (2012). Observing calving-generated ocean waves with coastal broadband seismometers, Jakobshavn Isbræ, Greenland. *Annals of Glaciology*, *53*(60), 79–84. https://doi.org/10.3189/2012/AoG60A200

Amundson, J. M., Fahnestock, M., Truffer, M., Brown, J., Lüthi, M. P., & Motyka, R. J. (2010). Ice mélange dynamics and implications for terminus stability, Jakobshavn Isbræ, Greenland. *Journal of Geophysical Research*, *115*(F1), F01005. https://doi.org/10.1029/2009JF001405

Amundson, J. M., Kienholz, C., Hager, A. O., Jackson, R. H., Motyka, R. J., Nash, J. D., & Sutherland, D. A. (2020). Formation, flow and break-up of ephemeral ice mélange at LeConte Glacier and Bay, Alaska. *Journal of Glaciology*, *66*(258), 577–590. https://doi.org/10.1017/jog.2020.29

Amundson, J. M., Truffer, M., Lüthi, M. P., Fahnestock, M., West, M., & Motyka, R. J. (2008). Glacier, fjord, and seismic response to recent large calving events, Jakobshavn Isbræ, Greenland. *Geophysical Research Letters*, *35*(22), L22501. https://doi.org/10.1029/2008GL035281

Benn, D. I., & Åström, J. A. (2018). Calving glaciers and ice shelves. *Advances in Physics X*, *3*(1), 1513819. https://doi.org/10.1080/23746149.2018.1513819

Benn, D. I., Todd, J., Luckman, A., Bevan, S., Chudley, T. R., Åström, J., et al. (2023). Controls on calving at a large Greenland tidewater glacier: Stress regime, self-organised criticality and the crevasse-depth calving law. *Journal of Glaciology*, *69*(278), 1–16. https://doi.org/10.1017/jog.2023.81

Benn, D. I., Warren, C. R., & Mottram, R. H. (2007). Calving processes and the dynamics of calving glaciers. *Earth-Science Reviews*, *82*(3), 143–179. https://doi.org/10.1016/j.earscirev.2007.02.002

Bézu, C., & Bartholomaus, T. C. (2024). Greenland ice sheet's distinct calving styles are identified in terminus change timeseries. *Geophysical Research Letters*, *51*(21), e2024GL110224. https://doi.org/10.1029/2024GL110224

Bonnet, P., Yastrebov, V. A., Queutey, P., Leroyer, A., Mangeney, A., Castelnau, O., et al. (2020). Modelling capsizing icebergs in the open ocean. *Geophysical Journal International*, *223*(2), 1265–1287. https://doi.org/10.1093/gji/ggaa353

Burton, J. C., Amundson, J. M., Abbot, D. S., Boghosian, A., Cathles, L. M., Correa-Legisos, S., et al. (2012). Laboratory investigations of iceberg capsize dynamics, energy dissipation and tsunamigenesis. *Journal of Geophysical Research*, *117*(F1), F01007. https://doi.org/10.1029/2011JF002055

Cowton, T., Slater, D., Sole, A., Goldberg, D., & Nienow, P. (2015). Modeling the impact of glacial runoff on fjord circulation and submarine melt rate using a new subgrid-scale parameterization for glacial plumes. *Journal of Geophysical Research: Oceans*, *120*(2), 796–812. https://doi.org/10.1002/2014jc010324

Cusack, J. M., Jackson, R. H., Nash, J. D., Skyllingstad, E., Pettit, E. C., Sutherland, D. A., et al. (2023). Internal gravity waves generated by subglacial discharge: Implications for tidewater glacier melt. *Geophysical Research Letters*, *50*(12), e2022GL102426. https://doi.org/10.1029/2022gl102426

De Pinho Dias, N., Leroyer, A., Mangeney, A., & Castelnau, O. (2025). Fluid-structure modeling of iceberg capsize. *Ocean Engineering*, *336*, 121765. https://doi.org/10.1016/j.oceaneng.2025.121765

Drazin, P. G., & Reid, W. H. (2004). *Hydrodynamic stability*. Cambridge University Press.

Edwards, T. L., Nowicki, S., Marzeion, B., Hock, R., Goelzer, H., Seroussi, H., et al. (2021). Projected land ice contributions to twenty-first-century sea level rise. *Nature*, *593*(7857), 74–82. https://doi.org/10.1038/s41586-021-03302-y

Eidam, E. F., Sutherland, D. A., Duncan, D., Kienholz, C., Amundson, J. M., & Motyka, R. J. (2020). Morainal bank evolution and impact on terminus dynamics during a tidewater glacier stillstand. *Journal of Geophysical Research: Earth Surface*, *125*(11), e2019JF005359. https://doi.org/10.1029/2019JF005359

Goliber, S., & Catania, G. (2024). Glacier terminus morphology informs calving style. *Geophysical Research Letters*, *51*(15), e2024GL108530. https://doi.org/10.1029/2024gl108530

Gräff, D., Lipovsky, B. P., Vieli, A., Dachauer, A., Jackson, R., Farinotti, D., et al. (2025). Calving-driven fjord dynamics resolved by seafloor fibre sensing. *Nature*, *644*(8076), 404–412. https://doi.org/10.1038/s41586-025-09347-7

Gregg, M. C., D'Asaro, E. A., Riley, J. J., & Kunze, E. (2018). Mixing efficiency in the ocean. *Annual Review of Marine Science*, *10*(1), 443–473. https://doi.org/10.1146/annurev-marine-121916-063643

Holland, D. M., & Jenkins, A. (1999). Modeling thermodynamic ice–ocean interactions at the base of an ice shelf. *Journal of Physical Oceanography*, *29*(8), 1787–1800. https://doi.org/10.1175/1520-0485(1999)029<1787:mtioia>2.0.co;2

Hubbard, B., Cook, S., & Coulson, H. (2009). Basal ice facies: A review and unifying approach. *Quaternary Science Reviews*, *28*(19–20), 1956–1969. https://doi.org/10.1016/j.quascirev.2009.03.005

Hunter, L. E., & Powell, R. D. (1998). Ice foot development at temperate tidewater margins in Alaska. *Geophysical Research Letters*, *25*(11), 1923–1926. https://doi.org/10.1029/98GL01403

Huss, M., & Hock, R. (2015). A new model for global glacier change and sea-level rise. *Frontiers in Earth Science*, *3*(54). https://doi.org/10.3389/feart.2015.00054

Jackson, R. H., Motyka, R. J., Amundson, J. M., Abib, N., Sutherland, D. A., Nash, J. D., & Kienholz, C. (2022). The relationship between submarine melt and subglacial discharge from observations at a tidewater glacier. *Journal of Geophysical Research: Oceans*, *127*(10), e2021JC018204. https://doi.org/10.1029/2021JC018204

Jackson, R. H., Nash, J. D., Kienholz, C., Sutherland, D. A., Amundson, J. M., Motyka, R. J., et al. (2020). Meltwater intrusions reveal mechanisms for rapid submarine melt at a tidewater glacier. *Geophysical Research Letters*, *47*(2), e2019GL085335. https://doi.org/10.1029/2019GL085335

James, T. D., Murray, T., Selmes, N., Scharrer, K., & O'Leary, M. (2014). Buoyant flexure and basal crevassing in dynamic mass loss at Helheim Glacier. *Nature Geoscience*, *7*(8), 593–596. https://doi.org/10.1038/ngeo2204

Kienholz, C., Amundson, J. M., Motyka, R. J., Jackson, R. H., Mickett, J. B., Sutherland, D. A., et al. (2019). Tracking icebergs with time-lapse photography and sparse optical flow, LeConte Bay, Alaska, 2016–2017. *Journal of Glaciology*, *65*(250), 195–211. https://doi.org/10.1017/jog.2018.105

Lüthi, M. P., & Vieli, A. (2016). Multi-method observation and analysis of a tsunami caused by glacier calving. *The Cryosphere*, *10*(3), 995–1002. https://doi.org/10.5194/tc-10-995-2016

MacAyeal, D. R., Abbot, D., & Sergienko, O. (2011). Iceberg-capsize tsunamigenesis. *Annals of Glaciology*, *52*(58), 51–56. https://doi.org/10.3189/172756411797252103

MacAyeal, D. R., Freed-Brown, J., Zhang, W. W., & Amundson, J. M. (2012). The influence of ice melange on fjord seiches. *Annals of Glaciology*, *53*(60), 45–49. https://doi.org/10.3189/2012/AoG60A027

Malles, J.-H., Maussion, F., Ultee, L., Kochtitzky, W., Copland, L., & Marzeion, B. (2023). Exploring the impact of a frontal ablation parameterization on projected 21st-century mass change for northern hemisphere glaciers. *Journal of Glaciology*, *69*(277), 1317–1332. https://doi.org/10.1017/jog.2023.19

Marzeion, B., Hock, R., Anderson, B., Bliss, A., Champollion, N., Fujita, K., et al. (2020). Partitioning the uncertainty of ensemble projections of global glacier mass change. *Earth's Future*, *8*(7), e2019EF001470. https://doi.org/10.1029/2019EF001470

McPhee, M. G., Maykut, G. A., & Morison, J. H. (1987). Dynamics and thermodynamics of the ice/upper ocean system in the marginal ice zone of the Greenland Sea. *Journal of Geophysical Research*, *92*(C7), 7017–7031. https://doi.org/10.1029/JC092iC07p07017

Meredith, M. P., Inall, M. E., Brearley, J. A., Ehmen, T., Sheen, K., Munday, D., et al. (2022). Internal tsunamigenesis and ocean mixing driven by glacier calving in Antarctica. *Science Advances*, *8*(47), eadd0720. https://doi.org/10.1126/sciadv.add0720

Nash, J. D., Marion, J., McComb, N., Nahorniak, J. S., Jackson, R. H., Perren, C., et al. (2017). Autonomous CTD profiling from the robotic oceanographic surface sampler. *Oceanography*, *30*(2), 110–112. https://doi.org/10.5670/oceanog.2017.229

Nash, J. D., Pettit, E. C., Shaya, M. F., & Jackson, R. H. (2025). Near-terminus ocean currents measured from ADCP moorings deployed using robotic boats at LeConte Glacier, Alaska, Sept 2018 [Dataset]. *Zenodo*. https://doi.org/10.5281/zenodo.16923006

O'Neel, S., Echelmeyer, K. A., & Motyka, R. J. (2003). Short-term variations in calving of a tidewater glacier: LeConte Glacier, Alaska, USA. *Journal of Glaciology*, *49*(167), 587–598. https://doi.org/10.3189/172756503781830430

Rabinovich, A. B. (2009). Seiches and harbor oscillations. In *Handbook of coastal and ocean engineering* (pp. 193–236). https://doi.org/10.1142/9789812819307_0009

Rounce, D. R., Hock, R., Maussion, F., Hugonnet, R., Kochtitzky, W., Huss, M., et al. (2023). Global glacier change in the 21st century: Every increase in temperature matters. *Science*, *379*(6627), 78–83. https://doi.org/10.1126/science.abo1324

Slater, D. A., Straneo, F., Das, S. B., Richards, C. G., Wagner, T. J. W., & Nienow, P. W. (2018). Localized plumes drive front-wide ocean melting of a Greenlandic tidewater glacier. *Geophysical Research Letters*, *45*(22), 12350–12358. https://doi.org/10.1029/2018GL080763

Sutherland, D. A., Jackson, R. H., Kienholz, C., Amundson, J. M., Dryer, W. P., Duncan, D., et al. (2019). Direct observations of submarine melt and subsurface geometry at a tidewater glacier. *Science*, *365*(6451), 369–374. https://doi.org/10.1126/science.aax3528

Sutherland, D. A., Jackson, R. H., Kienholz, C., Amundson, J. M., Dryer, W. P., Duncan, D., et al. (2020). Water temperature, salinity, currents, and others collected by conductivity, temperature and pressure (CTD) and acoustic Doppler current profiler (ADCP) from MV Steller and MV Pelican in LeConte Bay, Alaska from 2016-08-09 to 2018-09-18 (NCEI Accession 0189574) [Dataset]. *NSF Arctic Data Center*. https://doi.org/10.18739/A2WW77125

Tennekes, H., & Lumley, J. L. (1972). *A first course in turbulence*. The MIT Press. https://doi.org/10.7551/mitpress/3014.001.0001

Tsai, V. C., Rice, J. R., & Fahnestock, M. (2008). Possible mechanisms for glacial earthquakes. *Journal of Geophysical Research*, *113*(F3), F03014. https://doi.org/10.1029/2007JF000944

Wagner, T. J. W., Straneo, F., Richards, C. G., Slater, D. A., Stevens, L. A., Das, S. B., & Singh, H. (2019). Large spatial variations in the flux balance along the front of a Greenland tidewater glacier. *The Cryosphere*, *13*(3), 911–925. https://doi.org/10.5194/tc-13-911-2019

Walter, F., Olivieri, M., & Clinton, J. F. (2013). Calving event detection by observation of seiche effects on the Greenland fjords. *Journal of Glaciology*, *59*(213), 162–178. https://doi.org/10.3189/2013JoG12J118

Weiss, K. J., Nash, J. D., Wengrove, M. E., Osman, N., Cohen, N. F., Jackson, R. H., et al. (2025). Direct measurement of glacier ice melt: Boundary layer details are critical for submarine melt prediction at near-vertical ice faces. *Geophysical Research Letters*, *52*(11), e2025GL114952. https://doi.org/10.1029/2025GL114952

Williams, P. L., Burgess, D. O., Waterman, S., Roberts, M., Bertrand, E. M., & Bhatia, M. P. (2021). Nutrient and carbon export from a tidewater glacier to the coastal ocean in the Canadian arctic archipelago. *Journal of Geophysical Research: Biogeosciences*, *126*(9), e2021JG006289. https://doi.org/10.1029/2021JG006289

Zemp, M., Jakob, L., Dussaillant, I., Nussbaumer, S., Gourmelen, N., Dubber, S., et al. (2025). Community estimate of global glacier mass changes from 2000 to 2023. *Nature*, *639*(8054), 382–388. https://doi.org/10.1038/s41586-024-08545-z

Zhao, K. X., Stewart, A. L., & McWilliams, J. C. (2022). Linking overturning, recirculation, and melt in glacial fjords. *Geophysical Research Letters*, *49*(15), e2021GL095706. https://doi.org/10.1029/2021GL095706